Shock Wave Generation and Radiation from a Turbofan Engine Under Flow Distortion

Majd Daroukh, Cyril Polacsek, Alain Chelius

Shockwave Generation and Radiation from an UHBR Engine with Flow Distortion

M. Daroukh*, C. Polacsek †, and A. Chelius‡
DAAA, ONERA, Université Paris Saclay
F-92322 Châtillon - France

This paper presents aeroacoustic investigations on a full-scale Ultra High Bypass Ratio (UHBR) engine with inflow distortion at transonic conditions. Computational Fluid Dynamics (CFD) simulations are first realized to compute the shocks in the vicinity of the fan. These shocks are then radiated in the near-field thanks to Computational AeroAcoustics (CAA) simulations. The chaining between CFD and CAA simulations is done by injecting the shocks in terms of usual conservative variables using a non-reflecting boundary condition. The CAA solver is based on the non-linearized Euler equations which allows to define the CFD/CAA interface close to the fan where the propagation of shocks is highly non-linear. Both shock generation and propagation mechanisms are investigated and the effects of inflow distortion are highlighted by comparison with a baseline case without distortion. The flow distortion is shown to be responsible for a modification of shock amplitudes along the circumferential direction. Thus, azimuthal modes appear in addition to the rotor-locked mode present without distortion. A particular feature of the studied configuration is the presence of a supersonic flow region in the bottom part of the nacelle. This supersonic pocket blocks the shocks in the lower half of the nacelle and also modifies the angle at which they leave the nacelle in its upper half. Consequently, the far-field radiation (obtained using Kirchhoff's integral method) is mainly oriented skywards and towards the side of descending blades. Acoustic power estimates are provided to quantify these effects.

Nomenclature

a = speed of sound of the uniform far-field flow, m/s

a_0 = time-averaged speed of sound, m/s

B = number of rotor blades

CDC = circumferential distortion coefficient

*Research Engineer, Department of Aerodynamics, Aeroelasticity, and Aeroacoustics, majd.daroukh@onera.fr.
†Research Engineer, Department of Aerodynamics, Aeroelasticity, and Aeroacoustics, cyril.polacsek@onera.fr.
‡Research Engineer, Department of Aerodynamics, Aeroelasticity, and Aeroacoustics, alain.chelius@onera.fr.

d = source-observer distance used for far-field radiation, m

h = in-duct observer height, m

H = channel height (h/H being the normalized observer height), m

I_{nn} = normal component of acoustic intensity at BPFn on far-field sphere, W/m^2

I_{xn} = axial component of acoustic intensity at BPFn on in-duct planes, W/m^2

k_n = acoustic wavenumber at BPFn in the uniform far-field flow, 1/m

L = length of inlet duct, m

m = azimuthal mode order

M = Mach number of the uniform far-field flow

$\mathbf{M_0}$ = time-averaged Mach number vector of Cartesian coordinates (M_{x0}, M_{y0}, M_{z0})

n = BPF harmonic

$\mathbf{n}$ = normal vector on source surface with outside orientation

p_n = pressure fluctuations at BPFn, Pa

r_{95} = radial position at 95% of blade height, m

S = source surface for far-field radiation, m^2

$\mathbf{u_n}$ = velocity fluctuations vector at BPFn and of Cartesian coordinates (u_{xn}, u_{yn}, u_{zn}), m/s

U_{x0} = time-averaged axial velocity, m/s

V = number of stator vanes

$\mathbf{x}$ = observer position of Cartesian coordinates (x, y, z) or cylindrical coordinates (x, r, θ), m

$\mathbf{x'}$ = source position of Cartesian coordinates (x', y', z'), m

α = angle of attack, rad

β = Lorentz factor of the uniform far-field flow

ρ = density of the uniform far-field flow, kg/m^3

ρ_0 = time-averaged density, kg/m^3

σ = Lorentz-modified source-observer distance used for far-field radiation, m

ϕ = polar angle of far-field observer position, rad

Superscripts

$\bar{\cdot}$ = complex conjugate

I. Introduction

The motivation for reducing fuel consumption has driven the evolution of aeroengines towards higher bypass ratio architectures. The most recent ones, called Ultra High Bypass Ratio (UHBR), are equipped with very short asymmetric intakes which cannot make the entering flow uniform in the azimuthal direction. This flow heterogeneity (or distortion) is further amplified at operating conditions with non-zero angle of attack. This is typically the case during landing or take-off operations (angle of attack around 10°-15°) where airport neighbours are the most exposed to noise nuisance. Several recent studies have therefore focused on the impact of distortion on the noise emitted by turbofan engines [1–8]. They have shown that the tone noise characteristics can be significantly modified by: (a) introducing new acoustic sources caused by the distortion/fan blades interaction [3, 4, 8], (b) modifying the conventional fan-blade wakes/Outlet Guide Vanes (OGVs) interaction [3, 4, 7, 8], and (c) modifying the generation and propagation of fan-blade shocks at transonic speeds [1–3, 5, 6, 8].

The present paper focuses on that last point. Shockwave propagation has been extensively studied since the 1970s using analytical approaches. Morfey and Fisher first developed a 1D model for shock decay based on the linearized weak-shock theory [9]. McAlpine and Fisher wrote a 2D model in the frequency domain (the so-called FDNS model) where the shocks can have an arbitrary shape and where the decay is still predicted using Morfey and Fisher's model [10]. Many extensions of the FDNS model have then been proposed throughout the years [11–14]. As for shockwave generation, its modeling has been less adressed due to its complexity and only very recently a fully analytical model has been proposed [15]. To account for complex geometries and flows (such as distorted flow), numerical approaches are nevertheless still required. Shockwave generation and radiation can be estimated using a Computational Fluid Dynamics (CFD) solver in a one-simulation approach as proposed by recent studies [2, 5]. However, the associated computational cost is very high, especially if the radiation of acoustic waves is meant to be correctly captured over a long distance outside of the nacelle. Most of the numerical studies [1, 3, 6] are therefore based on a two-step methodology where the CFD solution is chained to a Computational AeroAcoustics (CAA) solver to propagate and radiate the shocks. The latter methodology is chosen here using the CFD/CAA chaining strategy developed by Thisse *et al.* where the shocks are injected in the CAA domain in terms of usual conservative variables using a non-reflecting boundary condition [16]. Another originality of the method is that the CAA part is done by solving the non-linearized Euler equations while the linearized ones are often adopted even for transonic cases with shocks (as in [3]). This approach allows to study separately the shock generation and the shock propagation mechanisms by defining the CFD/CAA chaining interface very close to the fan where the propagation of shocks is highly non-linear. The effects of inlet or liner design in the presence of a realistic source could therefore be easily investigated in the future with this methodology by repeating only the CAA simulation (as long as the coupling effects on shock generation can be discarded). The work of Thisse *et al.* [16] was the precursor validation step so that the present paper mainly focuses on the physical aspects of the effects of distortion on shockwave generation and radiation.

This study is carried out in the framework of a Clean Sky 2 European project (ASPIRE) for which a full-scale UHBR engine model has been designed. Since no stagger variation is included between the blades, the acoustic waves radiate at the Blade Passing Frequency (BPF) and its harmonics only (i.e. there is no multiple pure tone [17]). The effects of distortion on both shock generation and propagation are highlighted by comparing the results with a baseline case with a clean inflow (zero angle of attack).

A presentation of the turbofan model is first given in Sec. II. It is followed by a description of the numerical strategy in Sec. III, with a focus on the CFD/CAA chaining. Secs. IV and V show the effects of flow distortion on shock generation and shock radiation respectively. Acoustic power considerations are then given in Sec. VI to provide a quantitative measure of the impact of distortion on acoustics. Sec. VII finally adresses the main conclusions.

II. ASPIRE Turbofan Model and Operating Conditions

The ASPIRE fan stage includes an asymmetric intake with a small droop, $B = 16$ rotor blades, and $V = 36$ OGVs. The target bypass ratio is equal to 16 and the in-flight minimum thrust was chosen to be representative of a modern mid-sized passenger aircraft, with a nacelle radius around 1 meter. In order to simplify the numerical set-up and to reduce the computational cost, the droop is neglected and the simulations are performed using an axisymmetric intake shown in Fig. 1. Preliminary studies performed by NLR have shown that neglecting the droop has a little effect on inlet flow and shock generation and that the flow incidence was largely responsible for the significant changes with respect to the baseline case (with or without droop). The objective of the study is essentially focused on the outline of distortion effects on shock generation and radiation under critical conditions. An extreme angle of attack of 15° is therefore considered for the distortion case and the rotational speed is slightly increased above the nominal regime in order to ensure fully-propagating shockwaves in the intake. The investigated operating conditions are summarized in Table 1.

Table 1 Operating conditions with/without flow distortion.

	Baseline	Distortion
Fan rotation speed (vs. nominal regime)	108 %	108 %
Flight Mach number	0.27	0.27
Relative tip Mach number	1.14	1.14
Angle of attack	0°	15°

III. Numerical Strategy

A. CFD Simulation

The first step of the numerical methodology proposed here is the computation of fan-blade shocks thanks to a CFD simulation. It is done using the ONERA's CFD solver *elsA* which is based on a cell-centered finite volume approach on a structured multi-block grid [18]. The computational domains for baseline and distortion cases shown in Fig. 2 are

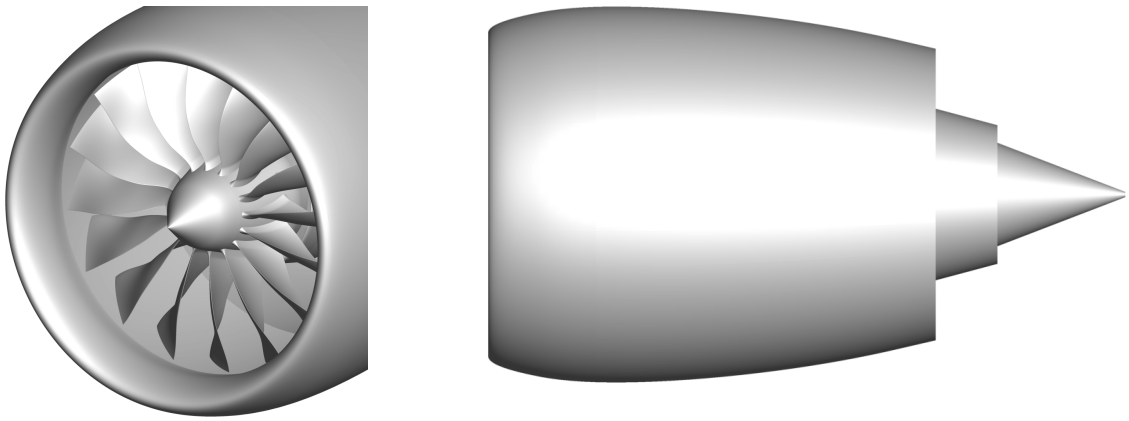

(a) Front view. (b) Side view.

Fig. 1 ASPIRE turbofan model.

restricted to the fan and the nacelle is approximated by a duct with suited inlet and outlet boundary conditions to reach the target values for inlet, bypass, and core mass flow (not given for confidentiality reasons).

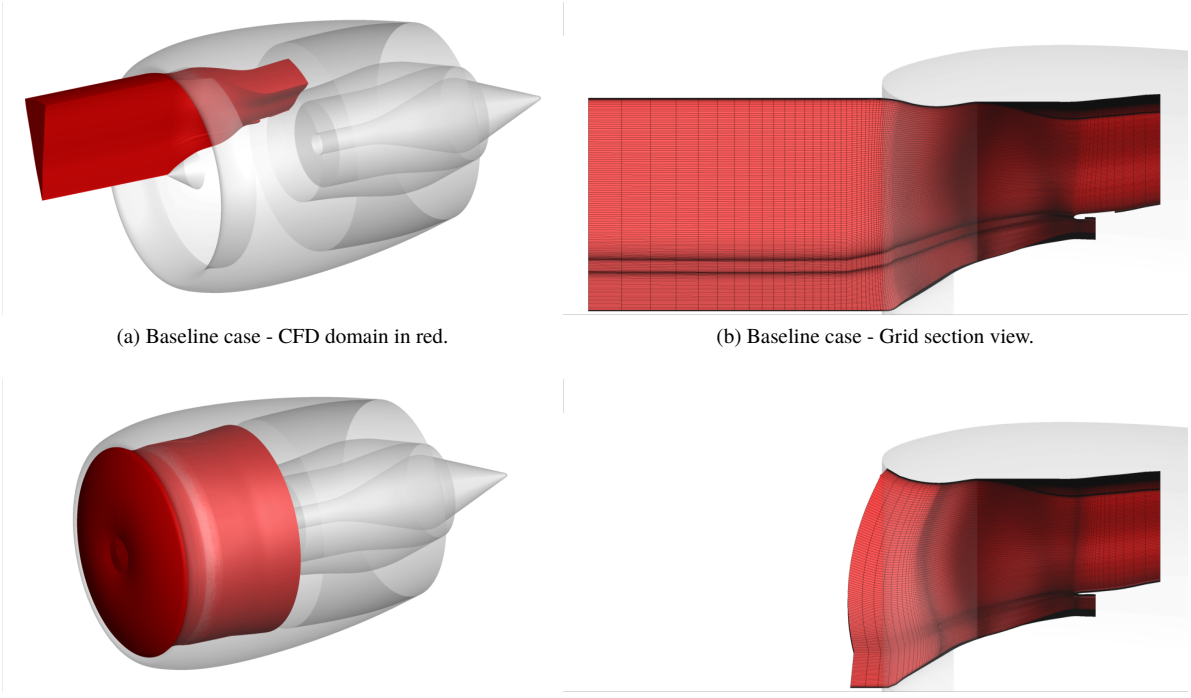

(a) Baseline case - CFD domain in red. (b) Baseline case - Grid section view.

(c) Distortion case - CFD domain in red. (d) Distortion case - Grid section view.

Fig. 2 CFD domains and grid section views.

For the baseline case, the Reynolds-Averaged Navier-Stokes (RANS) equations are solved in the rotating frame (the shocks are stationary in the rotating frame when there is no distortion). The turbulent quantities are determined

using k-ϵ two-equation model of Launder and Sharma [19], the spatial discretization is done with Roe scheme with Van Albada limiter (second-order accuracy) and the temporal one is based on a first-order backward Euler scheme. A single channel grid is computed and periodic conditions are used on the azimuthal boundaries. A wall-resolved mesh of about 15 million points is designed to capture the shock correctly around the fan blade (see Figs. 2a and 2b). The mesh is extended in the upstream direction to accurately propagate the N-waves up to the exit section and a stretching zone is added to limit numerical reflections at inlet boundary. The simulation is run on 69 cores and costs about 3000 CPUh in total.

For the distortion case, the unsteady RANS (uRANS) equations need to be solved since the shocks are no longer stationary in the rotating frame. As for the baseline case, Launder and Sharma k-ϵ turbulence model and Roe spatial scheme with Van Albada limiter are used. However, the time integration is based on a second-order Gear algorithm with 3600 time steps per fan rotation. A full-annulus and wall-resolved mesh grid of about 208 million points is designed to account for distortion (see Figs. 2c and 2d). Inflow distortion map at the nacelle entrance has been extracted from an uRANS computation of the whole nacelle-fan configuration performed by NLR [6], associated partner of ASPIRE project. This map is used as the inlet boundary condition (total pressure, total enthalpy, flow direction and turbulent variables are injected) and allows to restrict the uRANS computation with distortion to the in-duct domain. Therefore, the mesh cannot be extended in the upstream direction as done for the baseline case and the stretching is made closer to the fan. Finally, to prevent inaccuracies from the sliding mesh approach, the map is injected directly in the rotating frame by being rotated at each time step in the opposite direction of the fan rotation (possible because of the use of an axisymmetric intake). During the first three rotations, made on a coarse mesh (1 point over 2 in each direction), the outlet pressure is varied in order to get a mass flow rate as close as possible as the baseline one. Four more rotations are then needed on the fine mesh to converge the unsteady phenomena. The simulation is run over 448 cores and costs 75,000 CPUh in total (15,000 CPUh for the coarse mesh rotations and 60,000 CPUh for the fine mesh ones). After convergence, the mass flow rate of the distortion case is less than 1% higher than the one of the baseline case, which ensures a fair comparison between both cases. The total pressure ratio and the isentropic efficiency are found to be approximately 1% lower and 2% lower respectively because of distortion.

The distortion map provided by NLR is analyzed Fig. 3. The axial velocity contours are given in Fig. 3a and show how the flow incidence increases the flow velocity in the bottom part of the nacelle (around $\theta = -90°$). The radial evolution of distortion is plotted in Fig. 3b using the Circumferential Distortion Coefficient (CDC) applied to axial velocity [8]:

$$CDC(r) = \frac{\mathrm{Max}_\theta\,[\,U_{x0}(r,\theta)\,] - \mathrm{Min}_\theta\,[\,U_{x0}(r,\theta)\,]}{\mathrm{Mean}_\theta\,[\,U_{x0}(r,\theta)\,]}. \tag{1}$$

U_{x0} is the time-averaged axial velocity and $\mathrm{Min}_\theta\,[.]$, $\mathrm{Max}_\theta\,[.]$ and $\mathrm{Mean}_\theta\,[.]$ stand for the azimuthal minimum,

maximum and mean values respectively. The distortion increases with the radius and reaches very strong values (greater than 30%) close to the tip where the shocks are generated. The shape of distortion is further analyzed by extracting some azimuthal profiles at different channel heights (Fig. 3c where each profile is normalized by its mean value) and by computing the corresponding azimuthal Fourier components (Fig. 3d). The mean flow variations are almost sinusoidal as evidenced by the largely dominant spatial harmonic with circumferential order equal to 1 at all radial stations.

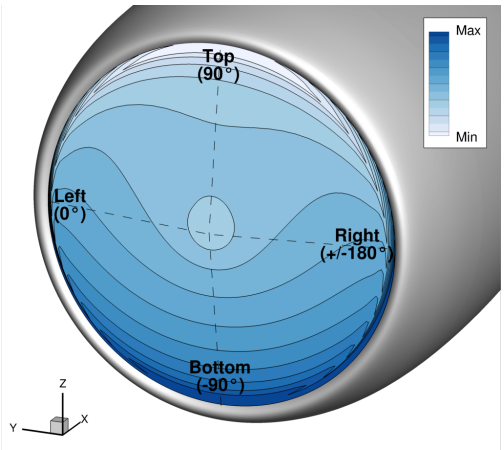

(a) Axial velocity contours.

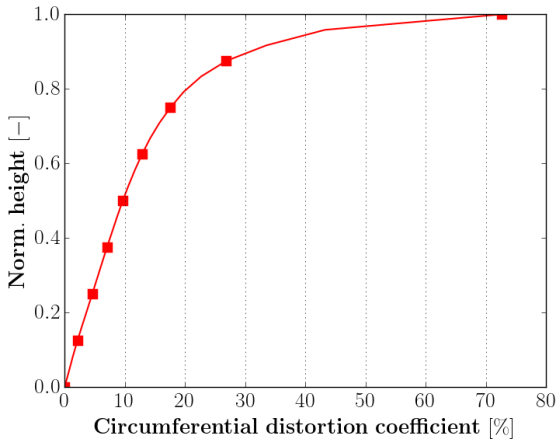

(b) Radial evolution of CDC.

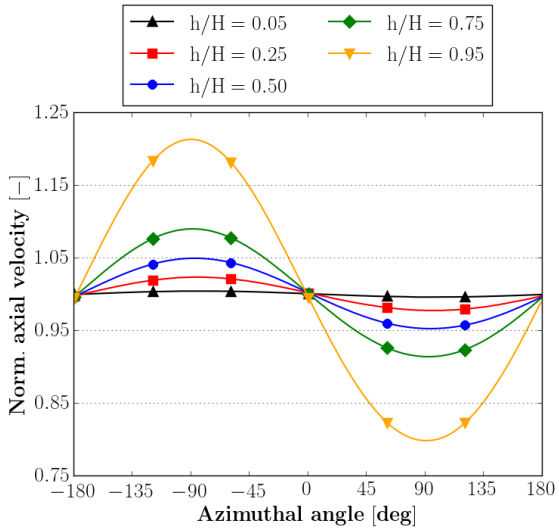

(c) Azimuthal profiles of axial velocity at different channel heights.

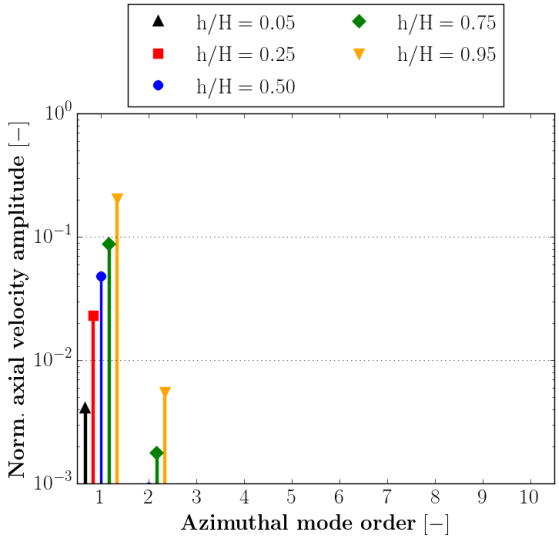

(d) Spatial harmonics of axial velocity at different channel heights.

Fig. 3 Inflow distortion map.

B. CAA Simulation

The second step of the proposed methodology is the propagation of shocks using a CAA solver. The *elsA* solver is used again by turning the RANS/uRANS mode into full Euler mode (non-linearized equations), viscous effects being

negligible for shock propagation. The CFD/CAA chaining method developed and validated by Thisse *et al.* [16] is used. The shock signature in the vicinity of the fan is extracted from the CFD and is injected in the CAA domain. The CFD/CAA interface is located at approximately half a chord from the rotor leading edge at 95% of blade height. The chaining is done for all conservative variables using Thompson non-reflecting boundary condition based on 1D characteristic equations [20]. A specific treatment is applied for converting the input data from the rotating frame (CFD solution) to the fixed frame (CAA frame).

The CAA domain is shown in Fig. 4a for a single channel. The computation is made on this single channel for the baseline case, with periodic conditions on azimuthal boundaries. For the distortion case, the same mesh is used and the domain is only duplicated over 360°. A coarsen grid section view (1 over 4 points) is given in Fig. 4b and shows the refined region. The grid is designed to correctly propagate upstream travelling waves up to BPF3 in the inlet region. This is ensured by axial and azimuthal discretizations of at least 30 points per wavelength at BPF3 (criterion based on academic studies of plane wave propagation through Cartesian grids using second order spatial schemes). The criterion is however relaxed in the radial direction because helicoidal waves are expected for propagation in circular ducts. Stretching zones are also added to avoid reflections on far-field boundaries. In total, the single channel grid totalizes 23 million points and the full-annulus one about 341 million points. Non-reflective boundary conditions are chosen at all fluid boundaries, Roe spatial scheme with Van Albada limiter (second-order accuracy) is used and time integration is based on a second-order Gear algorithm with 3600 time steps per fan rotation. For both simulations, four and half rotations are done to converge the acoustic fluctuations. The simulation is run over 128 cores and costs about 6000 CPUh for the baseline case. For the distortion case, 448 cores are used and the simulation costs about 60,000 CPUh. It is estimated that an equivalent one-simulation approach would have cost at least twice the combined cost of CFD and CAA simulations (cost of viscous terms, turbulence modeling and boundary layers points in the propagation domain).

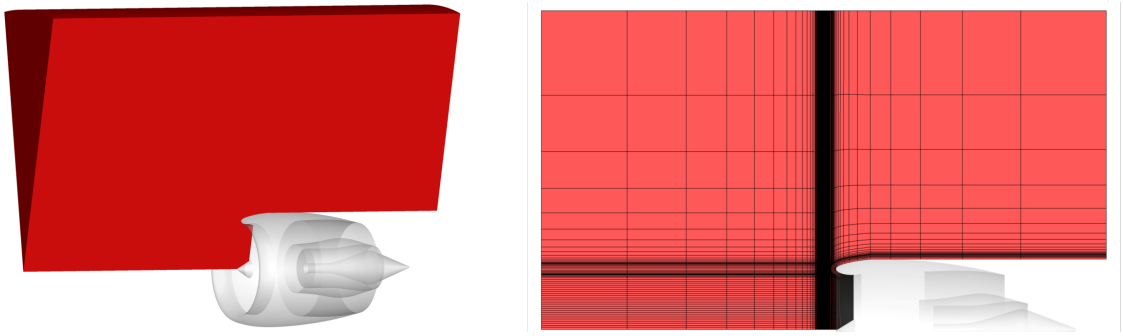

(a) CAA domain in red (single channel view).

(b) Grid section view (1 over 4 points).

Fig. 4 CAA domain and grid section view.

The behaviour of the CFD/CAA chaining method is checked for the baseline case in Fig. 5. The density field extracted from the CFD simulation at CFD/CAA interface location shown in Fig. 5a compares well with the one

extracted from the first cells of the CAA simulation given in Fig. 5b (the same scale is used). Azimuthal profiles of density (normalized by its mean value at 95% of channel height) are also given for some relevant radial stations in Fig. 5c and show very good agreement thus giving credit to the chosen strategy.

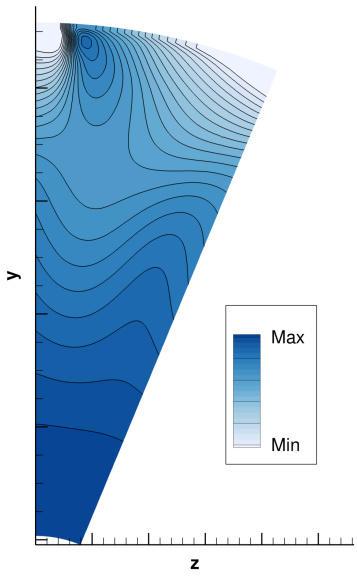

(a) Density extracted from CFD simulation at CFD/CAA interface location.

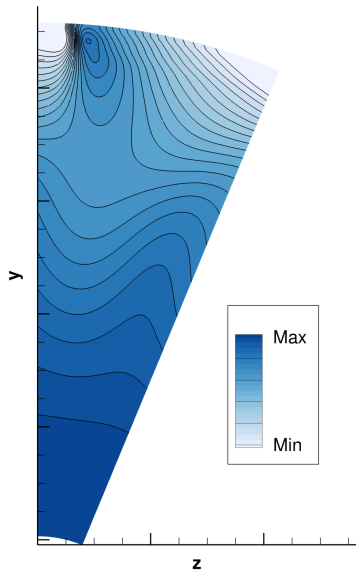

(b) Density extracted from CAA simulation at CFD/CAA interface location.

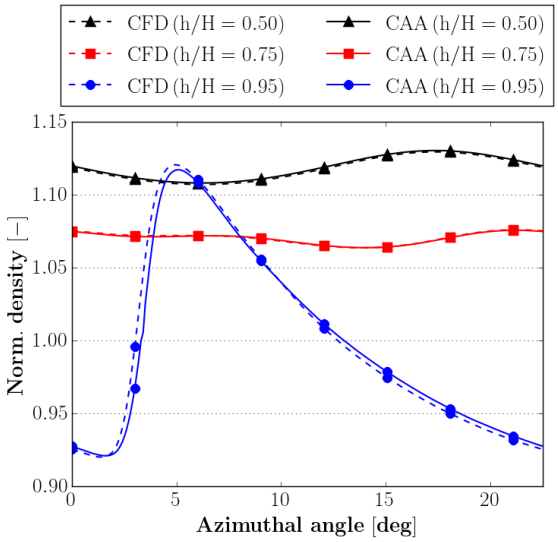

(c) CFD and CAA azimuthal profiles of density at CFD/CAA interface location for different channel heights.

Fig. 5 Validation of CFD/CAA chaining method on baseline case.

IV. Effects of Flow Distortion on Shockwave Generation

A. Flow Description around Fan-Blades

The focus is first put on the shock generation mechanism by analyzing the results of CFD simulations in the vicinity of fan blades. Contour plots of relative Mach number extracted at a radius close to the casing (corresponding to 95% of blade height and called r_{95} in the rest of the paper) are given in Figs. 6a and 6b for the baseline and the distortion case respectively. The maps are unwrapped to be represented in the $\theta - x$ axes, with θ the circumferential angle and x the engine axis (flow direction is from bottom to top in the plots). The axial position is normalized by the rotor chord at r_{95}, with 0 corresponding to the rotor leading edge. The converged RANS results of the baseline case are duplicated to be easily compared with the results of the distortion case. For the latter, an instantaneous solution is plotted at a time such that the top is located at $\theta = 90°$, the bottom at $\theta = -90°$, the left side at $\theta = 0°$ and the right side at $\theta = \pm 180°$ (such as in Fig. 3a). Here and in the rest of the paper, the baseline and distortion contour maps are always scaled in the same way. The acceleration of the flow along the suction side of the blades leading to the formation of the shocks is clearly observed. Around the top of the nacelle ($\theta = 90°$), the flow acceleration obtained with distortion is fairly close to the one observed for the baseline case. However, around the bottom of the nacelle ($\theta = -90°$), the flow is much more accelerated, which seems to modify the shape of the shocks. This flow acceleration can be related to the one observed on the distortion map shown in Fig. 3a.

Contour plots of density gradient magnitude are also given in Figs. 6c and 6d for both cases to better visualize the shocks. The shocks around the top ($\theta = 90°$) have a shape similar to the ones obtained without distortion. At the bottom ($\theta = -90°$), the flow acceleration makes the shocks appearing a bit closer to the trailing edge of the blades so that they are almost trapped inside the inter-blade channels.

B. Shock Analysis

For both cases, the flow fields are extracted at the same axial position in the vicinity of the fan to be injected into the CAA simulation. These flow fields contain the fan-blade shocks that will propagate inside the inlet duct and then radiate outside of the nacelle. They are analyzed here to provide a more detailed comparison between the shocks observed with and without distortion. The density fields obtained at this CFD/CAA interface location and expressed in the fixed frame (the one of the CAA simulation) are given in Fig. 7. The same iteration is represented and the field is duplicated over 360° for the baseline case to make the comparison easier. The potential effect of the fan is observed around mid-span and the shocks emerge close to the tip. The shocks seem to be much stronger in the baseline case and a strong heterogeneity of the shocks is observed with distortion. In particular, the shocks in the bottom region are weaker than the ones in the top.

This is further analyzed by extracting some probes over a full revolution from both simulations (note that the data injected in the CAA simulation is unsteady even for the baseline case since it is rotated at each time step to be expressed

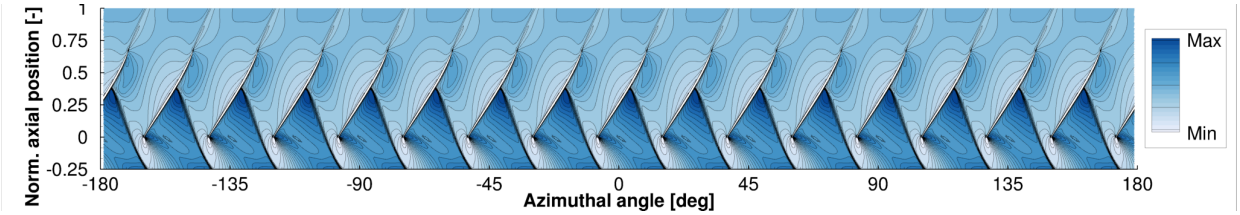

(a) Baseline case (duplicated field) - Relative Mach number.

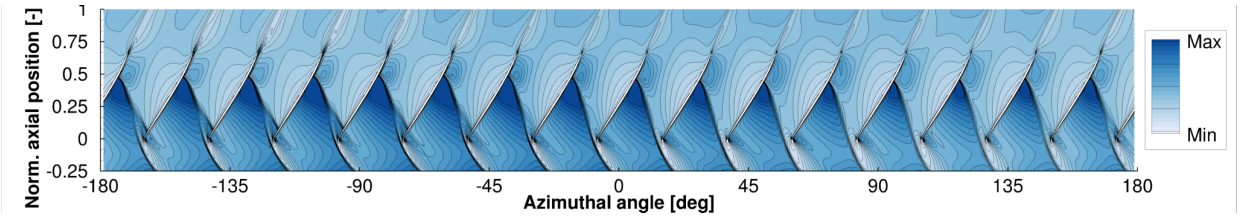

(b) Distortion case (instantaneous field) - Relative Mach number.

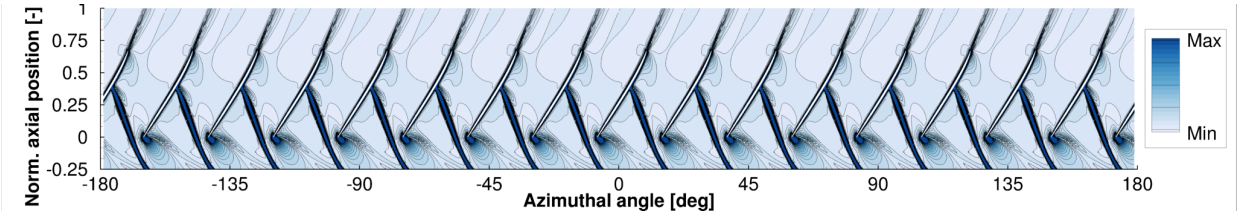

(c) Baseline case (duplicated field) - Density gradient magnitude.

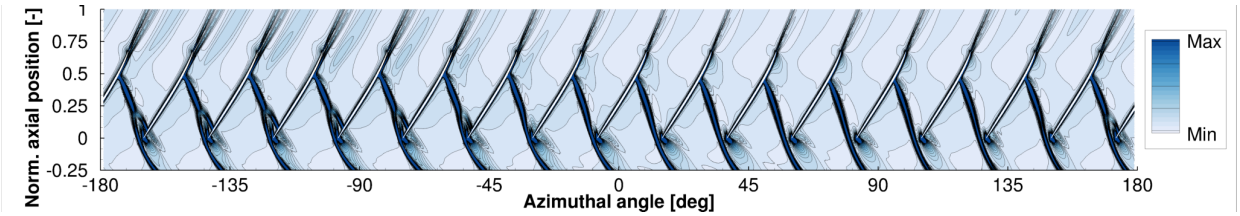

(d) Distortion case (instantaneous field) - Density gradient magnitude.

Fig. 6 Contour maps extracted at $r = r_{95}$.

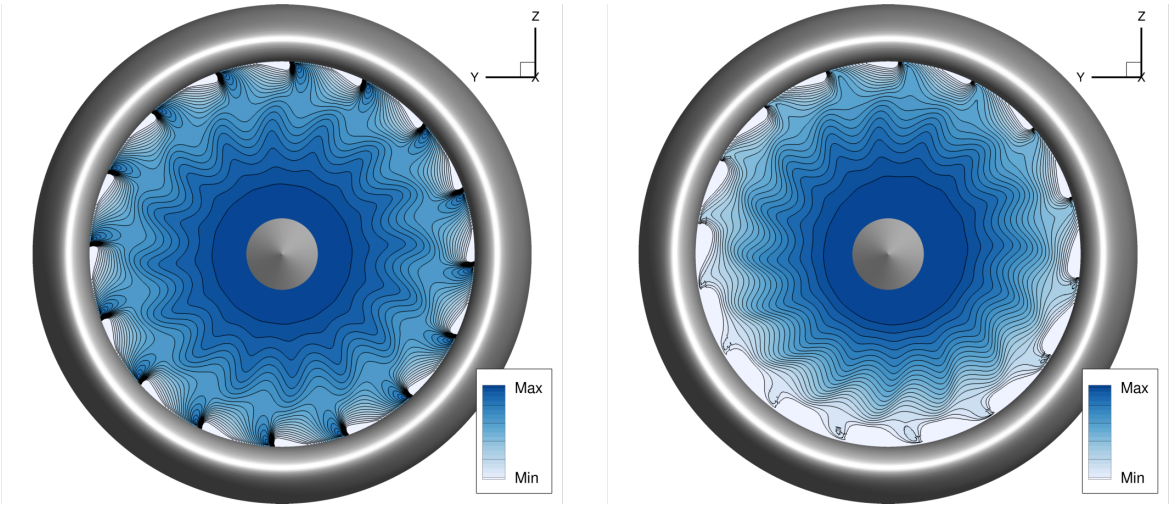

(a) Baseline case (duplicated field). (b) Distortion case.

Fig. 7 Density contours at the CFD/CAA chaining interface.

in the fixed frame). The static pressure signals obtained at 4 different azimuthal positions ($\theta = -180°$, $\theta = -90°$, $\theta = 0°$ and $\theta = 90°$) and at $r = r_{95}$ are represented in Fig. 8a. Only one curve is shown for the baseline case because it remains the same for the 4 positions (there is no time-shift since the probes are spaced by 90°, which is exactly the space between 4 blades). All curves are normalized by the mean value of the pressure signal obtained without distortion. N-waves are observed and the amplitude of the shocks is effectively lower with distortion (almost two times lower at some positions). The strong heterogeneity between the different azimuthal positions in terms of amplitude is emphasized. A time-shift that can be linked to the different shock angles is also present because of distortion. As expected, the fluctuations are found to remain at the BPF and its harmonics even in the presence of distortion. This is evidenced in Fig. 8b which shows the time Fourier transform of the precedent signals. Only the harmonics that are multiple of the number of blades (i.e. the BPF harmonics) emerge. This would have been different if some stagger variation was included between the blades as in [6].

The pressure field at BPF1 over the whole CFD/CAA chaining interface is now plotted in Fig. 9. The higher levels are reached close to the casing where the shocks appear. Lower amplitudes are found when there is distortion and this can be related to the weaker shocks. The heterogeneity is again observed with higher amplitudes in the top region.

This heterogeneity is further analyzed in Fig. 10 where the azimuthal Fourier components computed at $r = r_{95}$ are given. Again, results are normalized by the mean value of the pressure signal obtained without distortion at this position. Only the rotor-locked mode $m = nB = 16$ (n being the number of the BPF harmonic considered, here 1) appears for the baseline case. However, the distortion is responsible for the emergence of other modes close the rotor-locked one. Most of the signal is described by the rotor-locked mode and the distortion-rotor interaction modes $m = nB \pm 1$ and

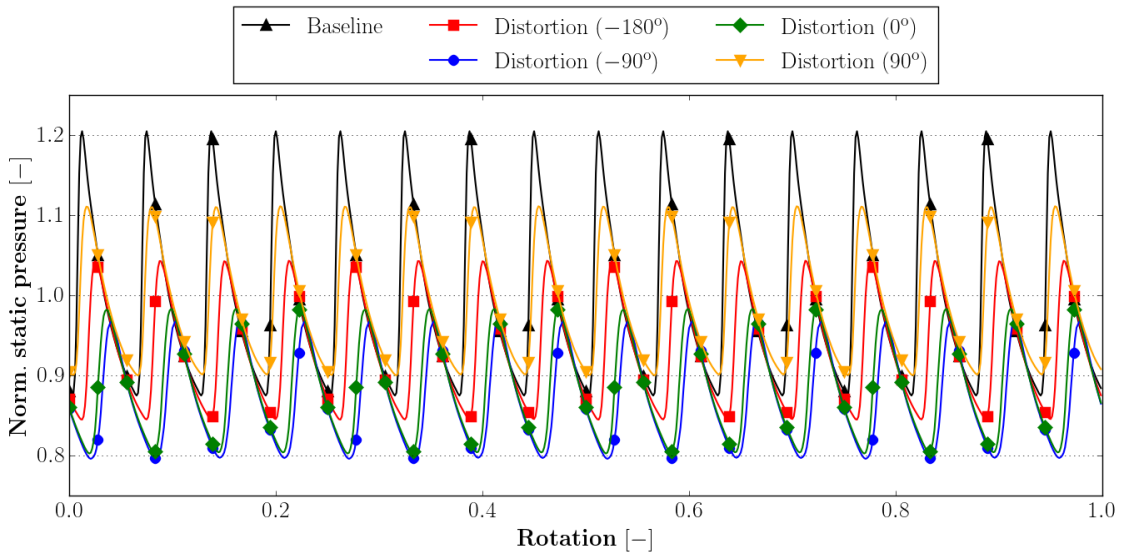

(a) Time signals.

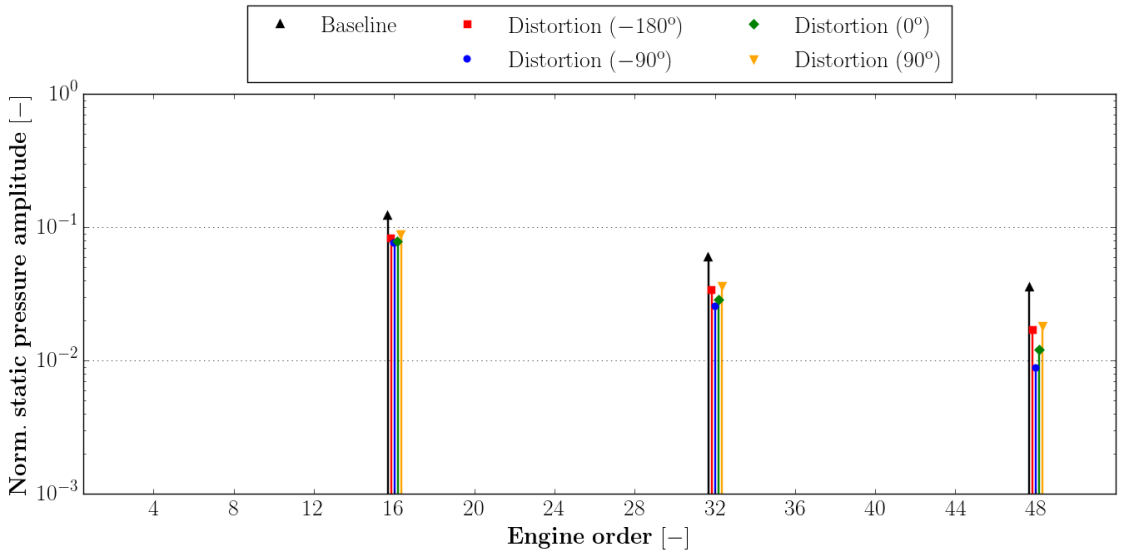

(b) Time Fourier transforms.

Fig. 8 Pressure time signal and Fourier transform at 4 different azimuthal positions and at $r = r_{95}$.

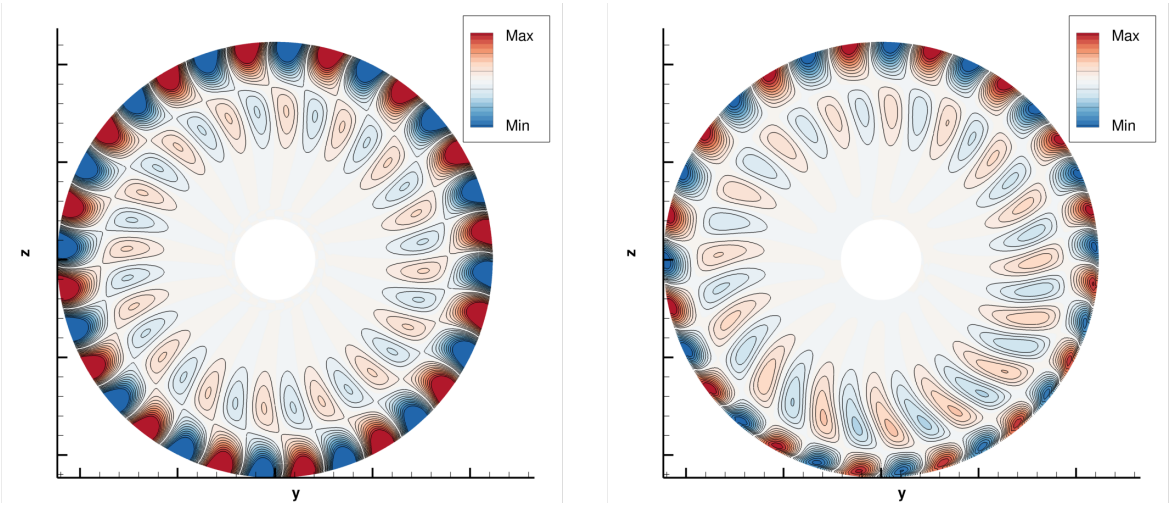

(a) Baseline case (duplicated field). (b) Distortion case.

Fig. 9 Contour maps of pressure real part at BPF1 on the CFD/CAA chaining interface.

$m = nB \pm 2$ which are related to the harmonics of distortion shown in Fig. 3d. Similar observations can be done at other BPFs.

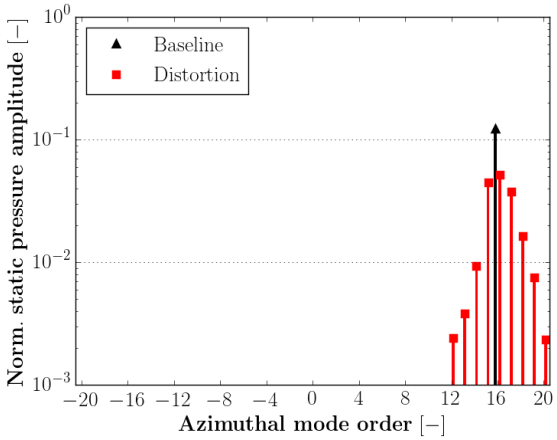

Fig. 10 Azimuthal mode distribution at $r = r_{95}$ at BPF1.

V. Effects of Flow Distortion on Shockwave Radiation

A. Mean Flow inside and around the Nacelle

The in-duct propagation of shocks and their radiation is now investigated. The mean flow obtained from CAA simulations is first analyzed in the nacelle in Fig. 11 where time-averaged axial Mach number contours are plotted for the baseline and distortion cases. Only one slice is shown for the baseline case (in Fig. 11a) since the mean flow is

axisymmetric (note that the slice has been duplicated for comparison purposes). For the distortion case, two slices have been represented: one vertical slice at $y = 0$ m in Fig. 11b and one horizontal slice at $z = 0$ m in Fig. 11c. The last contour level (dark blue) corresponds to 1. The flow acceleration around the casing is observed in all slices but is much more pronounced in the distortion case at the bottom of the nacelle ($\theta = -90°$) where a supersonic pocket is created. This is an effect of the flow incidence combined with the ultra short inlet duct [21]. It is also worth to note that the mean flow is symmetric in the horizontal plane.

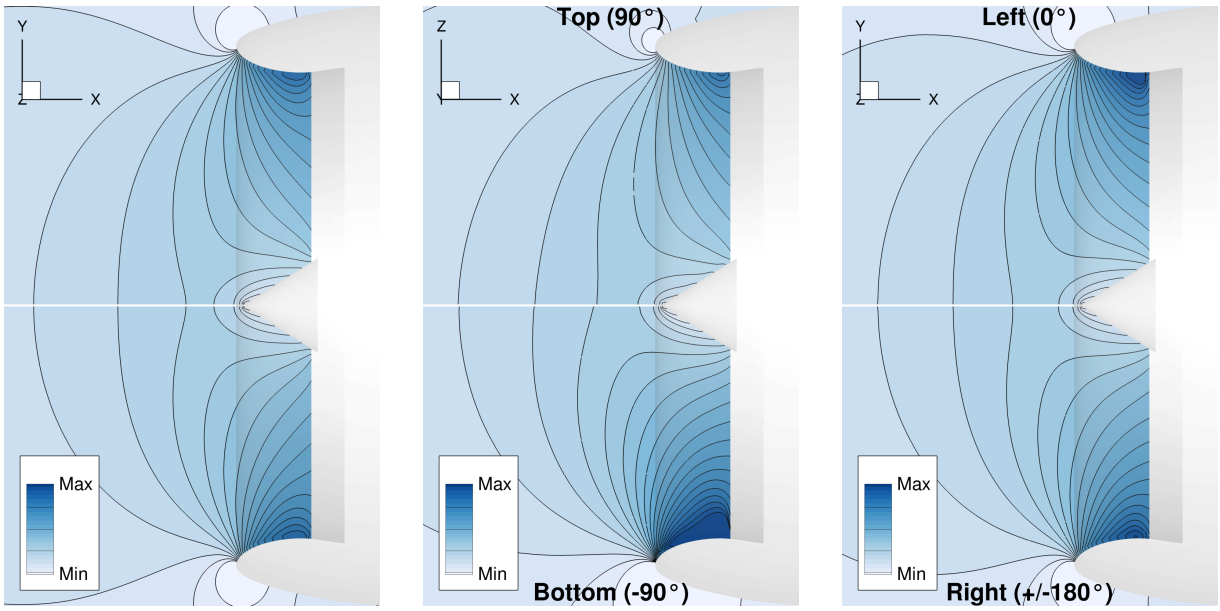

(a) Baseline case (duplicated field) - Symmetric slice.

(b) Distortion case - Slice $y = 0$ m.

(c) Distortion case - Slice $z = 0$ m.

Fig. 11 Contour maps of time-averaged axial Mach number on different slices.

B. In-Duct Propagation of Shocks

The focus is now put precisely on the propagation of shocks inside the inlet duct. This is done by plotting contour maps of density gradient magnitude at $r = r_{95}$ as in Figs. 6c and 6d, but from the CAA simulations instead of the CFD simulations. Results are given in Figs 12a and 12b for the baseline and the distortion case respectively. The top of the plots corresponds to the position of the CFD/CAA interface (location right upstream of the fan) and the bottom of the plots to the exit of the nacelle. A severe reduction of the shock amplitude during in-duct propagation is observed for the baseline case and can be related to the strong reduction of Mach number in the nacelle [22]. The distortion dramatically modifies the shock propagation in the inlet duct. The strongest impact is observed in the lower half of the nacelle (approximately from $\theta = -180°$ to $\theta = 0°$) where the shocks completely disappear. The curve plotted in red is the isoline corresponding to an axial Mach number of 1. It shows that this behaviour is due to the supersonic flow

region which pushes back the fan-blade shocks. The shocks therefore leave the nacelle in its upper half only and they are characterized by very different strengths and angles.

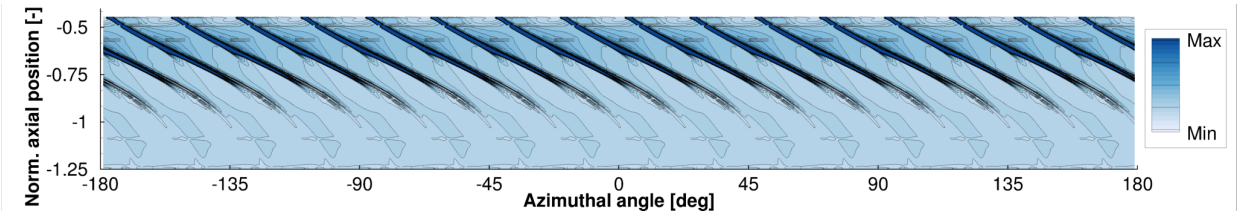

(a) Baseline case (duplicated field).

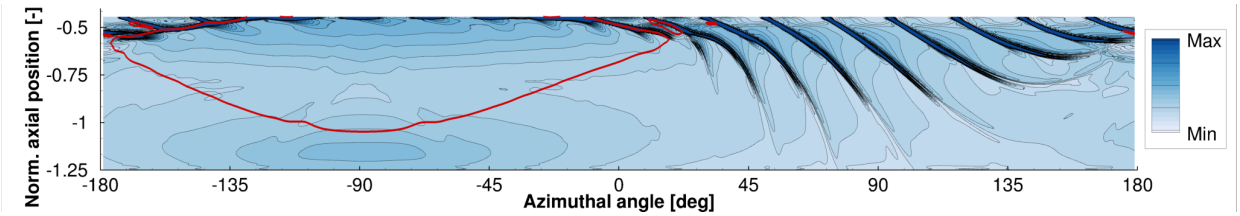

(b) Distortion case.

Fig. 12 Contour maps of instantaneous density gradient magnitude and sonic isoline in red at $r = r_{95}$.

These differences in shock angles are responsible for different directions of propagation of the associated acoustic waves. This is shown in Fig. 13 where pressure real part contours at BPF1 are plotted on the same slice and for both cases. It can be observed that the pressure waves propagate in the direction that crosses the shocks. Consequently, they leave the nacelle with an angle that depends on the circumferential position. Between $\theta = 0°$ and $\theta = 45°$ (upper left side), the wavefronts are almost aligned with the x-axis, leading to waves that propagate essentially along the azimuthal direction. On the contrary, between $\theta = 135°$ and $\theta = 180°$ (upper right side), the wavefronts are almost aligned with the θ-axis and the waves propagate essentially along the axial direction.

The high heterogeneity of the acoustic field during in-duct propagation can be expressed in terms of azimuthal modes. Azimuthal profiles of the pressure field at BPF1 are extracted at $r = r_{95}$ and at three axial positions (one close to the fan, one in the middle of the inlet duct, and one close to the nacelle exit) and a spatial Fourier transform is computed to determine the dominant modes. Results are presented in Fig. 14 for both baseline and distortion cases. They are normalized by the mean value of the pressure obtained without distortion at $r = r_{95}$ and at the axial position close to the fan. For the baseline case, only the rotor-locked mode $m = nB = 16$ appears along the inlet. The presence of distortion introduces a lot of new azimuthal modes with decreasing amplitudes when going farther from the rotor-locked mode. Close to the fan, most of the signal is described by the rotor-locked mode and the distortion-rotor interaction modes $m = nB \pm 1$ and $m = nB \pm 2$ as discussed before. But the signal is spread over more and more modes along the propagation such that almost all modes between -20 and 20 are within one order of magnitude close to the nacelle exit. This is partly due to the scattering of the modes over neighbour modes because of distortion but it is also a consequence

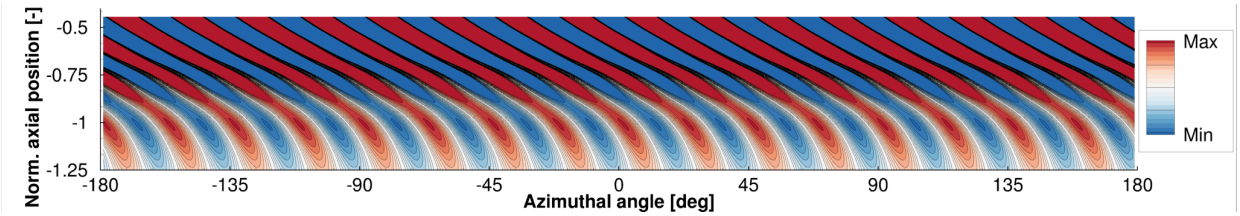

(a) Baseline case (duplicated field).

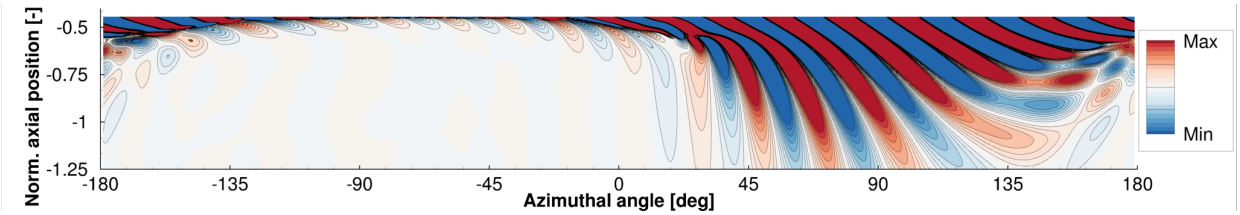

(b) Distortion case.

Fig. 13 Contour maps of pressure real part at $r = r_{95}$ at BPF1.

of the blockage of shocks in the bottom part of the nacelle which breaks down the rotating mode analysis.

C. Near-Field Radiation of Shocks

The near-field acoustic radiation is now investigated in Figs. 15, 16 and 17 where contours maps of pressure real part in the vicinity of the nacelle inlet are plotted at BPF1, BPF2, and BPF3 respectively. For each BPF, only one slice is represented for the baseline case because of its symmetry while two slices are plotted for the distortion case such as in Fig. 11: one vertical slice at $y = 0$ m and one horizontal slice at $z = 0$ m. For all BPFs and without distortion, the radiation is oriented to the sides (i.e. far from the axis) because of the relative high order of the rotor-locked mode which is the only existing mode. The waves propagate over smaller distance with increasing BPF because of the stretching zone. In the presence of distortion, the radiation is strongly heterogeneous in both the vertical and the horizontal planes. The heterogeneity in the vertical plane is first discussed. Because of the blockage of shocks in the bottom part of the nacelle, the radiation is clearly oriented to the top (or the sky), with very low levels obtained towards the bottom (or the ground). The pressure waves that exit the nacelle from its top are more oriented in the upstream direction than in the baseline case because of the presence of lower order modes. Interferences in the radial direction also occur which indicates the presence of radial modes of order higher than 1. The radiation is also heterogeneous in the horizontal plane, which is less expected given the symmetry of the mean flow on this plane (see Fig. 11c). This is to be related to the different angles of the shocks that leave the nacelle. On the upper right side (around $\theta = \pm 180°$), the pressure waves propagate essentially along the axial direction at the nacelle exit (see Fig. 13b) and this gives rise to a straight upstream radiation. On the contrary, on the upper left side, the pressure waves propagate mainly along the azimuthal direction when leaving the nacelle (see Fig. 13b) and the radiation is thus oriented towards the side. It is important to note that the left and right sides are only distinguished by the direction of rotation of the fan: the left side is the side of descending

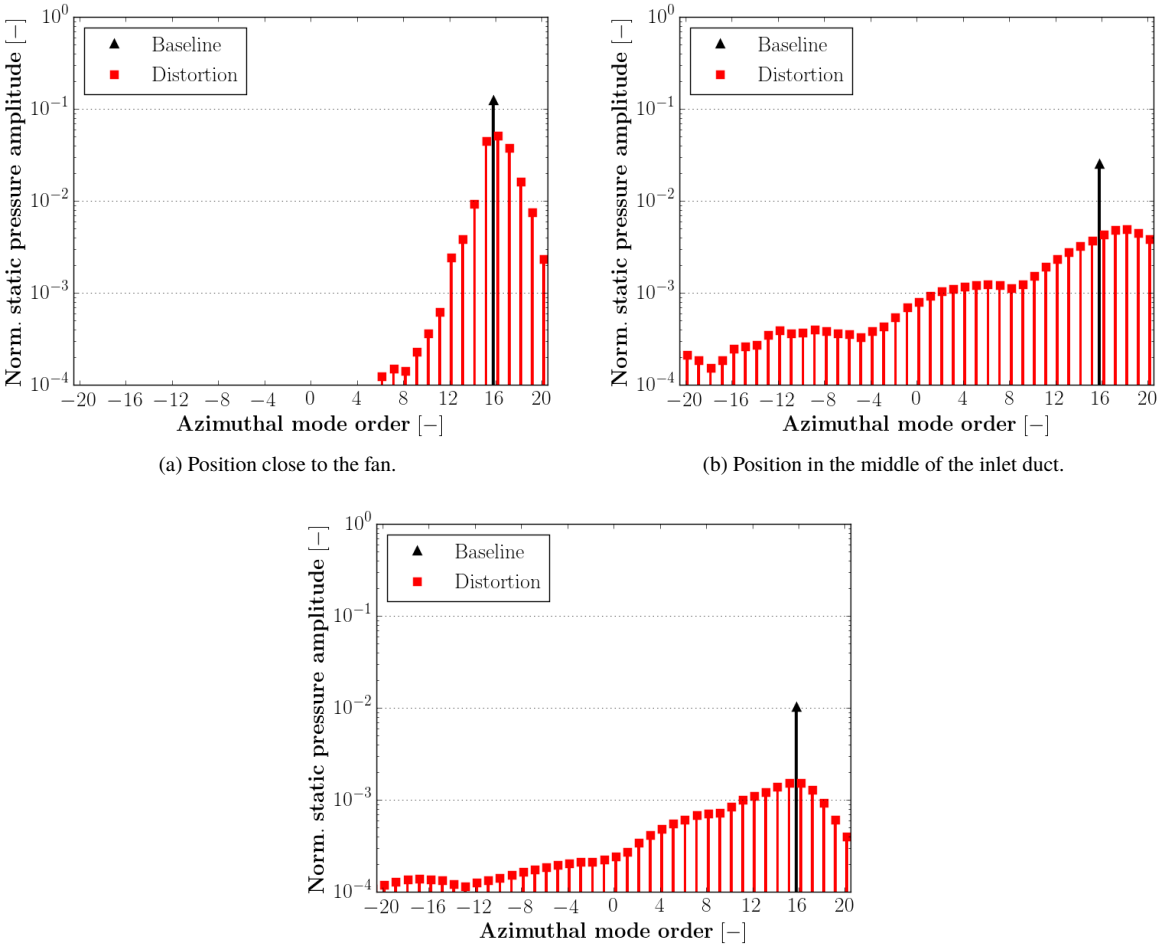

(a) Position close to the fan.

(b) Position in the middle of the inlet duct.

(c) Position close to the nacelle exit.

Fig. 14 Azimuthal mode distribution at BPF1 for different axial positions and at $r = r_{95}$.

blades while the right side is the side of ascending blades (the fan rotates in the clockwise direction here). Since the engines of current aircraft rotate in the same direction for economic reasons, the radiation of all the engines considered together is expected to be even more heterogeneous. In addition, the cabin would be unevenly exposed to shock noise for such configurations.

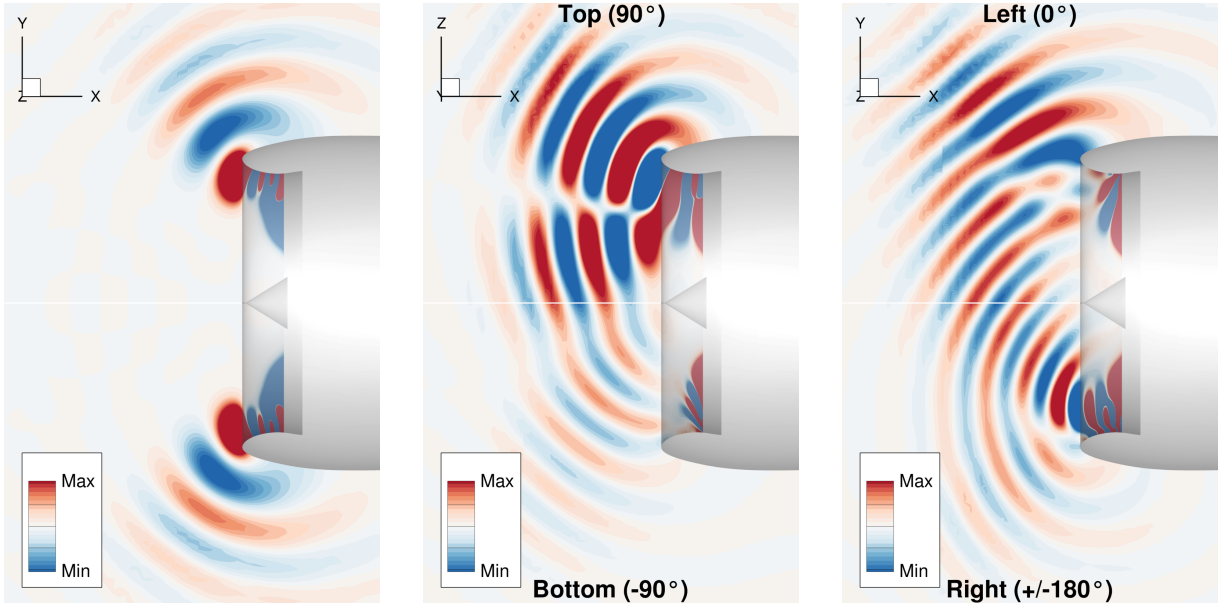

(a) Baseline case (duplicated field) - Symmetric slice.

(b) Distortion case - Slice $y = 0$ m.

(c) Distortion case - Slice $z = 0$ m.

Fig. 15 Contour maps of pressure real part on different slices in the near-field at BPF1.

VI. Acoustic Power Considerations

A. In-Duct Acoustic Power

Quantitative noise estimates are now proposed through acoustic power evaluation. In-duct acoustic power is first computed by integration of the axial component of intensity over successive x-planes. Cantrell & Hart's formulation is used for the intensity, its axial component $I_{xn}(\mathbf{x})$ at point $\mathbf{x}$ and at BPFn therefore writes [23]:

$$\begin{aligned} I_{xn}(\mathbf{x}) = p_n(\mathbf{x})\,\overline{u_{xn}}(\mathbf{x}) + M_{x0}(\mathbf{x}) \left[\frac{|p_n(\mathbf{x})|^2}{\rho_0(\mathbf{x})\,a_0(\mathbf{x})} + M_{x0}(\mathbf{x})\,p_n(\mathbf{x})\,\overline{u_{xn}}(\mathbf{x}) + \rho_0(\mathbf{x})\,a_0(\mathbf{x})\,|u_{xn}(\mathbf{x})|^2 \right] \\ + M_{y0}(\mathbf{x}) \left[M_{x0}(\mathbf{x})\,p_n(\mathbf{x})\,\overline{u_{yn}}(\mathbf{x}) + \rho_0(\mathbf{x})\,a_0(\mathbf{x})\,u_{xn}(\mathbf{x})\,\overline{u_{yn}}(\mathbf{x}) \right] \\ + M_{z0}(\mathbf{x}) \left[M_{x0}(\mathbf{x})\,p_n(\mathbf{x})\,\overline{u_{zn}}(\mathbf{x}) + \rho_0(\mathbf{x})\,a_0(\mathbf{x})\,u_{xn}(\mathbf{x})\,\overline{u_{zn}}(\mathbf{x}) \right]. \end{aligned} \tag{2}$$

$\mathbf{M_0} = (M_{x0}, M_{y0}, M_{z0})$, ρ_0 and a_0 are the time-averaged Mach number vector, density and speed of sound respectively. $\mathbf{u_n} = (u_{xn}, u_{yn}, u_{zn})$ and p_n are the velocity vector and pressure fluctuations at BPFn. This formulation, valid for

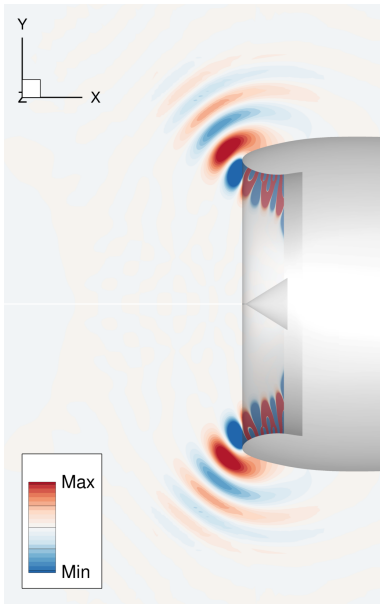

(a) Baseline case (duplicated field) - Symmetric slice.

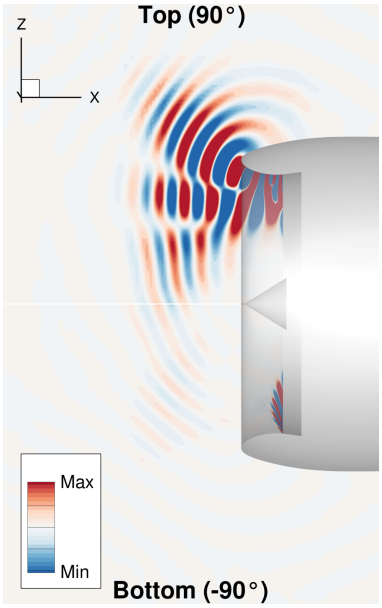

(b) Distortion case - Slice $y = 0$ m.

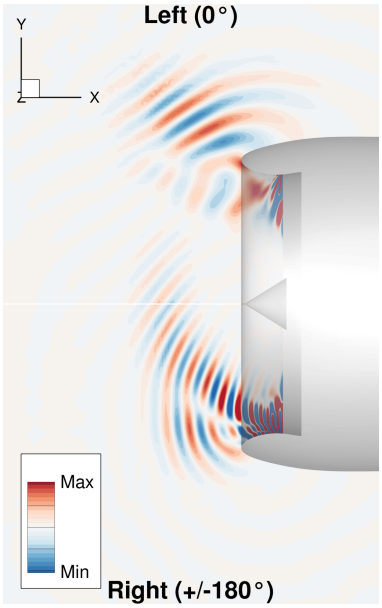

(c) Distortion case - Slice $z = 0$ m.

Fig. 16 Contour maps of pressure real part on different slices in the near-field at BPF2.

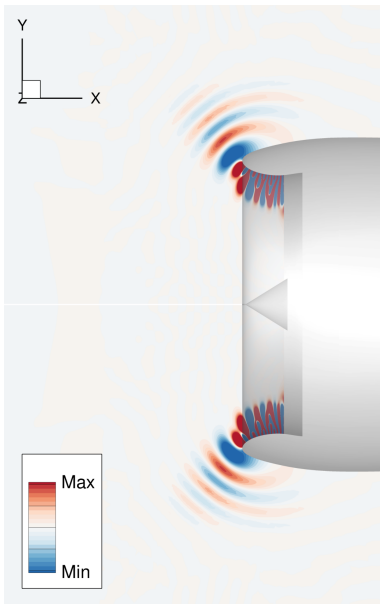

(a) Baseline case (duplicated field) - Symmetric slice.

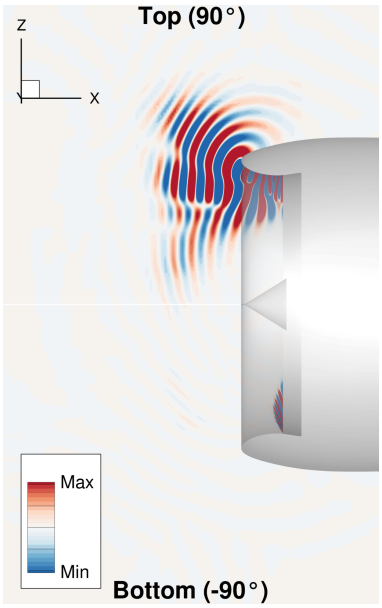

(b) Distortion case - Slice $y = 0$ m.

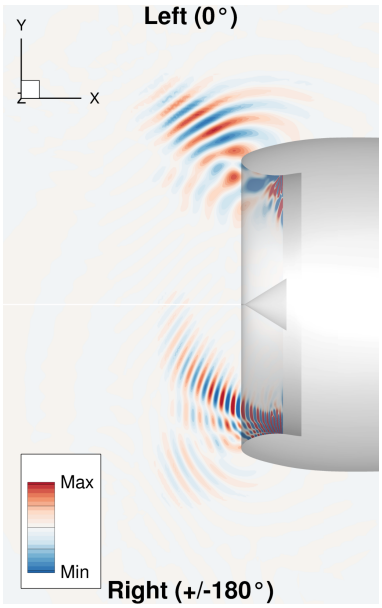

(c) Distortion case - Slice $z = 0$ m.

Fig. 17 Contour maps of pressure real part on different slices in the near-field at BPF3.

isentropic and irrotational flows, is the most used in the context of turbomachinery noise [17]. The mean flow is generally assumed to be axial (second and third lines are removed) but the full expression is kept here to account for the vertical component of the mean flow caused by the incidence. Because of the shocks present in the studied configuration, the flow is not isentropic and the acoustic power is not expected to be conserved in the non-linear region.

The procedure is applied on the CAA fields resulting from both cases. Results are given in Fig. 18 for the first three BPFs. The axial position is measured from the fan plane location and is expressed in terms of L, the length of the inlet duct (0 corresponds to the fan plane while $-L$ corresponds to the inlet plane). Close to the fan, the power levels are much stronger in the baseline case, with 5 to 10 dB differences at all BPFs. This is related to the weaker shocks experienced in the distortion case (see Fig. 8a). The power levels then decrease while going upstream but in different ways. For the baseline case, the evolution is irregular and the attenuation between the fan plane and the inlet plane is very high (around -25 dB for all BPFs). This is linked to the non-linear propagation of the shocks which are the only contributor to the power (the rotor-locked mode is the only existing mode, see Fig. 14). For the distortion case, the evolution is smoother and the attenuation is weaker (around -15 dB for all BPFs). In addition to the non-linear propagation of shocks, cut-on modes also propagate in this case (distortion-rotor interaction modes) and contribute to the power, which might explain these differences. At the inlet plane, the breakdown is therefore inverted and the power levels are higher in the presence of distortion (+3.5 dB at BPF1 and BPF2 and +5 dB at BPF3).

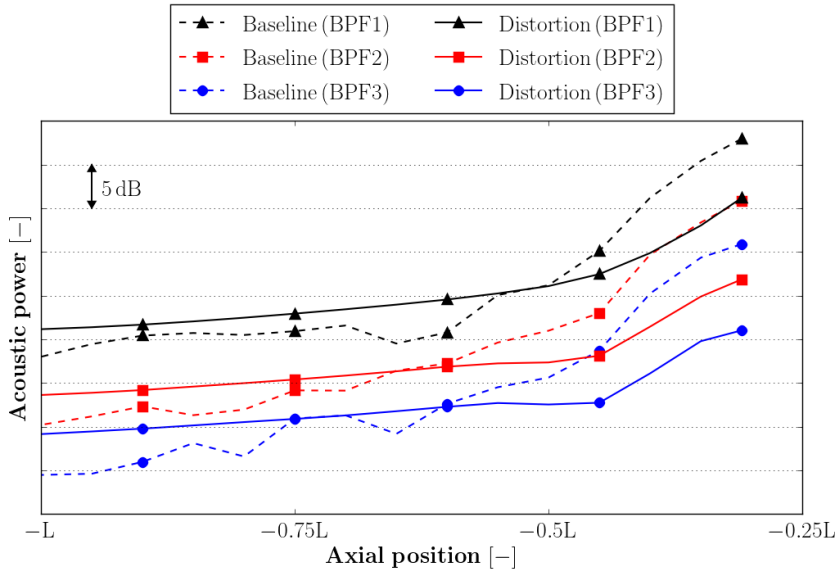

Fig. 18 Axial evolution of in-duct acoustic power.

B. Far-Field Acoustic Power

The focus is now put on the far-field acoustic power, which can differ from the in-duct acoustic power if the dominant modes have a low radiation efficiency or if some cut-off modes reach the inlet plane with a significant level [24]. The Kirchhoff's integral method is applied in the frequency-domain to get the far-field pressure at BPFn from the pressure field on a source surface S at the same frequency [25, 26]. One should note that solving the equation of Ffowcs Williams and Hawkings [27] is not needed when focusing on the sound radiation by the intake. For an observer point $\mathbf{x} = (x, y, z)$, the pressure at BPFn $p_n(\mathbf{x})$ therefore writes [25]:

$$p_n(\mathbf{x}) = \int_S \frac{1}{4\pi\, d(\mathbf{x},\mathbf{x}')} \left[M^2\, n_x(\mathbf{x}')\, \frac{\partial p_n}{\partial x}(\mathbf{x}') - \frac{\partial p_n}{\partial n}(\mathbf{x}') \right.$$
$$\left. + \left\{ i\, k_n \left(M\, n_x(\mathbf{x}') + \frac{\mathbf{n}(\mathbf{x}')\cdot(\mathbf{x}-\mathbf{x}')}{d(\mathbf{x},\mathbf{x}')} \right) + \beta^2\, \frac{\mathbf{n}(\mathbf{x}')\cdot(\mathbf{x}-\mathbf{x}')}{d(\mathbf{x},\mathbf{x}')^2} \right\} p_n(\mathbf{x}') \right] e^{-i\, k_n\, \sigma(\mathbf{x},\mathbf{x}')}\, dS(\mathbf{x}'). \tag{3}$$

The flow is assumed to be uniform and aligned with the x-axis. M is the Mach number, $\beta = \sqrt{1-M^2}$ is the Lorentz factor, ρ is the density, a is the speed of sound and $k_n = 2\pi\,\mathrm{BPFn}\,/a$ is the acoustic wavenumber. $\mathbf{x}' = (x', y', z')$ corresponds to a source point and $\mathbf{n}(\mathbf{x}')$ is its normal vector oriented outside of the source surface. $d(\mathbf{x},\mathbf{x}') = \sqrt{(x-x')^2 + \beta^2(y-y')^2 + \beta^2(z-z')^2}$ is the source-observer distance in the translating propagation medium and $\sigma(\mathbf{x},\mathbf{x}') = \left[d(\mathbf{x},\mathbf{x}') - M\,(x-x')\right]/\beta^2$ is the Lorentz-modified source-observer distance. For the distortion case, a change of frame is first required before applying the formula in order to have the infinite flow aligned with the x-axis (rotation of α around the y-axis, α being the angle of attack). Another change of frame is then needed to express the resulting far-field data in the nacelle frame (rotation of $-\alpha$ around the y-axis).

The method is applied from a source surface (shown in Fig. 19) that encloses the upstream part of the nacelle. The resulting sound pressure level at BPF1 on a far-field sphere is given in Fig. 20 for illustration (the contour levels are spaced by 2.5 dB). Three different views are shown for both cases: one view from the side, one view from the front and one view from the bottom. The main directivity patterns depicted in the near-field radiation results are found again in those contour maps. The radiation gathers in the fan plane for the baseline case while it is oriented in the upstream direction and towards the sky in the presence of distortion. The heterogeneity in the horizontal plane is highlighted in the front view maps with the left side levels ($\theta = 0°$) significantly higher than the right side ones ($\theta = \pm 180°$). Interferences that can be attributed to the high number of propagating modes in the presence of distortion are also observed.

The far-field pressure being known, the far-field power can now be evaluated by integration of the associated intensity over a spherical surface. The normal component of the far-field intensity $I_{nn}(\mathbf{x})$ at point $\mathbf{x}$ (of polar angle ϕ) and at BPFn is given by [28]:

$$I_{nn}(\mathbf{x}) = \frac{|p_n(\mathbf{x})|^2}{\rho\, a} \left[\frac{1 + M^2\cos^2(\phi-\alpha)}{\sqrt{1-M^2\sin^2(\phi-\alpha)}} + \left(1 + \frac{1}{1-M^2\sin^2(\phi-\alpha)} \right) M\cos(\phi-\alpha) \right]. \tag{4}$$

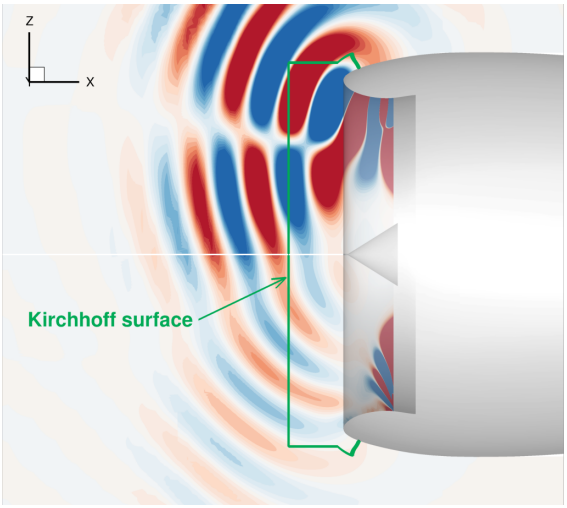

Fig. 19 Source surface used for Kirchhoff's integral method.

The resulting power is given for the first three BPFs and for both cases in Fig. 21, where it is compared to the in-duct power evaluated at the inlet plane (postion $-L$ in Fig. 18). The levels obtained are almost identical which is expected because the most powerful modes (i.e. the rotor-locked mode and the distortion-rotor interaction modes) are cut-on at this operating condition. The only difference between in-duct power and far-field power is seen at BPF3 for the baseline case (in-duct power higher by 2 dB). It is probably explained by numerical dissipation in the CAA simulation that occurs before reaching the source surface used for Kirchhoff's integral method. For the baseline case, the radiation is indeed strongly oriented towards the side where the mesh is not as fine as in the upstream direction. This is not observed in the distortion case because the waves are mainly radiated in the upstream direction with distortion. The far-field results at BPF3 should therefore be interpreted with caution and the following discussions will be limited to BPF1 and BPF2. The far-field acoustic power penalty induced by distortion at BPF1 and BPF2 is of 4 dB, which is in close agreement with the in-duct acoustic power penalty (3.5 dB).

The results given above only compare the total acoustic power resulting from both configurations. Analyzing the directivity is also important given the high heterogeneity of the radiation in the presence of distortion. This is done here by integrating the far-field intensity given by Eq. (4) over different half-spheres to compare their contribution on the total power. Four half-spheres (top, bottom, left and right half-spheres) are considered. The results for the top/bottom and left/right comparisons are given in Figs. 22a and 22b respectively. For the baseline case, since the radiation is axisymmetric, the power is equally distributed between all parts. This is no longer the case in the presence of distortion, where the top (or the sky) levels are 4 dB higher than the bottom (or the ground) ones at BPF1 and BPF2. As already mentionned, this is due to the blockage of shocks by the supersonic flow region in the bottom part of the nacelle. The penalty induced by distortion in terms of ground power is accordingly reduced to approximately 2 dB at these frequencies. The difference between left and right radiation is even more pronounced with the left levels roughly 9

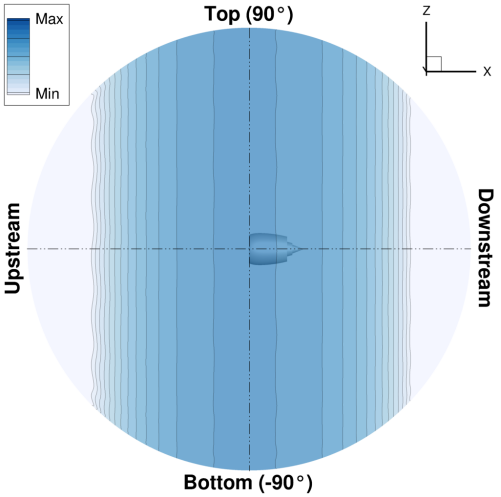

(a) Baseline case - Side view.

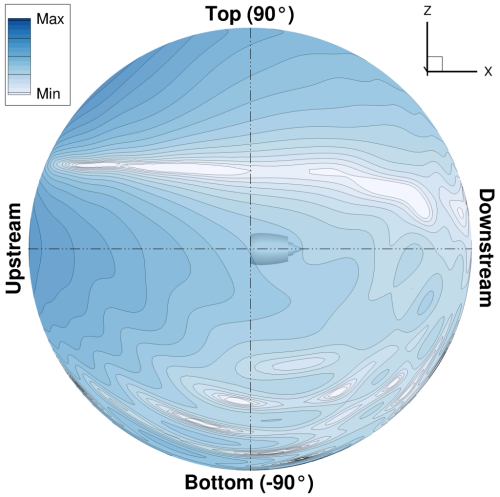

(b) Distortion case - Side view.

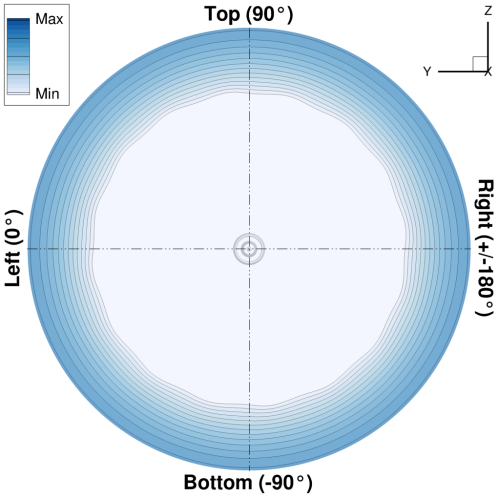

(c) Baseline case - Front view.

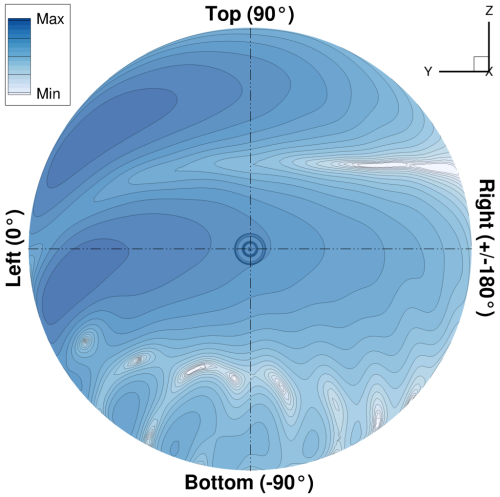

(d) Distortion case - Front view.

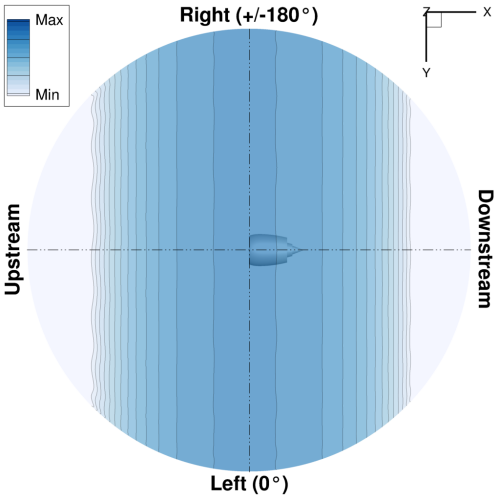

(e) Baseline case - Bottom view.

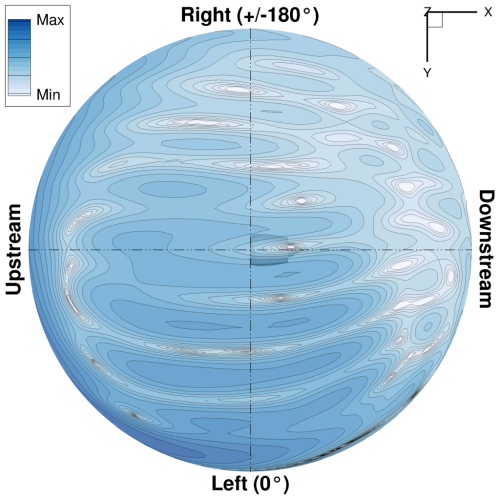

(f) Distortion case - Bottom view.

Fig. 20 Contour maps of sound pressure level on far-field sphere at BPF1.

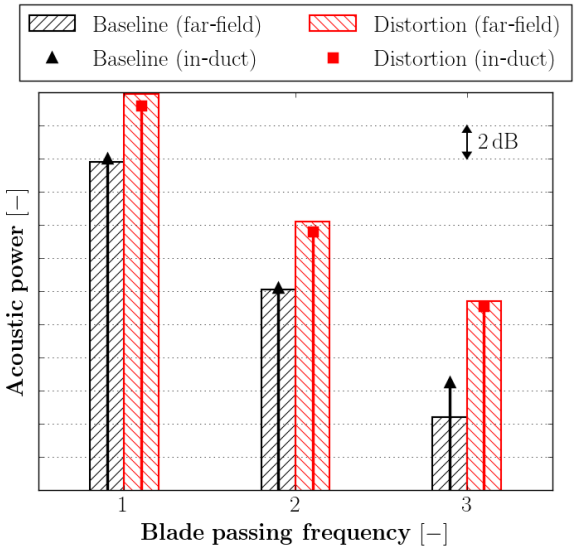

Fig. 21 In-duct and far-field acoustic power.

dB higher than the right ones. The cabin noise would therefore be much stronger on the side that faces the descending blades for such conditions where a supersonic pocket develops in the bottom part of the nacelle.

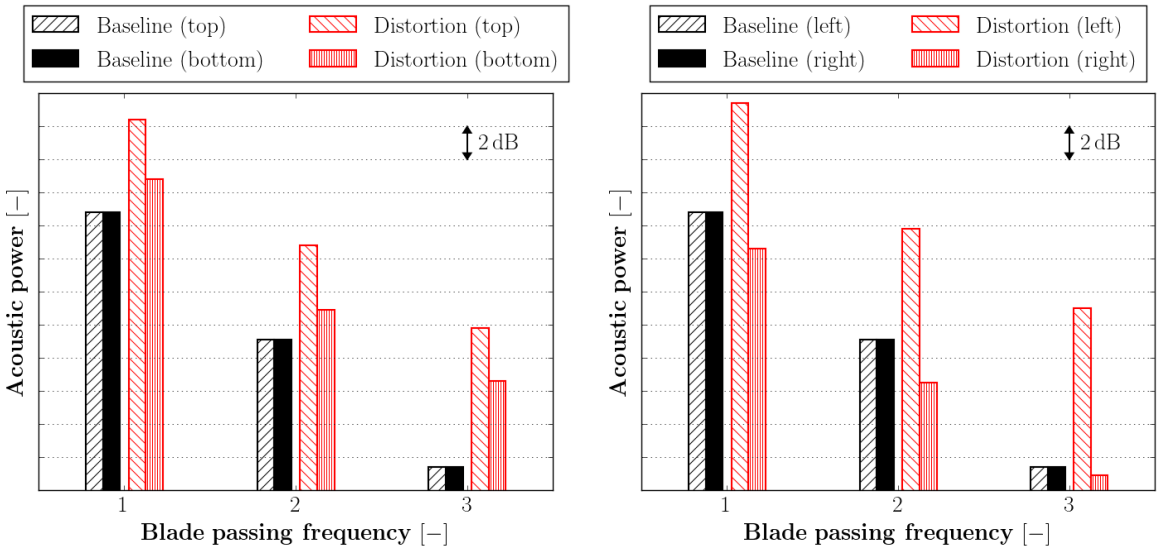

(a) Top and bottom.

(b) Left and right.

Fig. 22 Contribution of the different parts on the far-field acoustic power.

VII. Conclusion

Shockwave generation and radiation from an UHBR engine with inflow distortion has been investigated using a CFD/CAA chaining method. The shocks are extracted from a CFD simulation and are injected in the CAA domain in terms of conservative variables using a non-reflecting boundary condition. The CAA is based on the non-linearized Euler equations which allows to study the shock generation and the shock propagation mechanisms separately by putting the CFD/CAA interface close to the fan where the flow is highly non-linear. Inlet or liner (in the future) design optimization could therefore be done in the presence of a realistic source by repeating only the CAA simulation. The chaining method is shown to behave correctly on a baseline case without distortion and is then applied to the case with distortion.

Results on both shock generation and radiation have been provided and the effects of distortion were highlighted by comparing both cases. It is shown that the distortion strongly influences the generation of shocks in terms of strength and position. In the vicinity of the fan, the pressure field at the BPFs is no more described only by the rotor-locked mode since distortion-rotor interaction modes also appear. The number of contributing modes increases while the shocks propagate in the inlet duct. A very important feature of the studied configuration is the presence of a supersonic flow region in the bottom part of the nacelle, which is a combined effect of the flow incidence and the ultra short inlet. This supersonic pocket blocks the shocks in the lower half of the nacelle and also modifies the angle at which the shocks leave the nacelle in its upper half. Consequently, the radiation is strongly oriented skywards and towards the side of descending blades while it is axisymmetric without distortion. These effects have been quantified through acoustic power estimates. The in-duct power is increased by almost 4 dB at the first three BPFs in the presence of distortion. Far-field radiation using Kirchhoff's integral method has also been used to evaluate the contribution of the different directions on the total power. The integrated skywards intensity is 4 dB higher than the integrated groundwards intensity at the first BPFs in the presence of distortion. The difference between the sides is even more dramatic with levels 9 dB higher towards the side of descending blades.

The skywards characteristic of the radiation may be a good news in the scope of acoustic certification. However, because the left and right engines rotate in the same direction in current aircraft for economic reasons, the difference between the descending-blade and the ascending-blade sides would lead to an uneven exposure to shock noise for the cabin. If the priority is cabin noise reduction, and if a supersonic pocket is expected, then contra-rotating engines should be used in order to have the ascending blades of both engines oriented towards the fuselage. Only the isolated engine case was considered here, and accounting for its interaction with the wing might temper these conclusions.

Acknowledgments

ONERA carried out this study in the framework of the ASPIRE project in close cooperation with partners Airbus, NLR, and DLR. It has received funding from the Clean Sky 2 Joint Undertaking under the European Union's H2020

program (grant agreement no. 681856).

References

[1] Winkler, J., Reimann, C. A., Reba, R. A., and Gilson, J., "Turbofan Inlet Distortion Noise Prediction with a Hybrid CFD-CAA Approach," *20th AIAA/CEAS Aeroacoustics Conference*, 2014. doi:10.2514/6.2014-3102.

[2] Doherty, M., and Namgoong, H., "Impact of Turbofan Intake Distortion on Fan Noise Propagation and Generation," *22nd AIAA/CEAS Aeroacoustics Conference*, 2016. doi:10.2514/6.2016-2841.

[3] Winkler, J., Reimann, C. A., Gumke, C. D., Ali, A. A., and Reba, R. A., "Inlet and Aft Tonal Noise Predictions of a Full-Scale Turbofan Engine with Bifurcation and Inlet Distortion," *23rd AIAA/CEAS Aeroacoustics Conference*, 2017. doi:10.2514/6.2017-3034.

[4] Daroukh, M., Moreau, S., Gourdain, N., Boussuge, J.-F., and Sensiau, C., "Effect of Distortion on Turbofan Tonal Noise at Cutback with Hybrid Methods," *International Journal of Turbomachinery, Propulsion and Power*, Vol. 2, No. 3, 2017, p. 16. doi:10.3390/ijtpp2030016.

[5] Milidonis, K. F., Hynes, T., Doherty, M., and Namgoong, H., "The Effect of Steady Intake Distortion on Fan MPT Noise Under Sideline Flight Conditions," *24th AIAA/CEAS Aeroacoustics Conference*, 2018. doi:10.2514/6.2018-4188.

[6] Laban, M., Kok, J. C., and Brouwer, H. H., "CFD/CAA Analysis of UHBR Engine Tonal Noise," *24th AIAA/CEAS Aeroacoustics Conference*, 2018. doi:10.2514/6.2018-3780.

[7] Guérin, S., and Holewa, A., "Fan tonal noise from aircraft aeroengines with short intake: A study at approach," *International Journal of Aeroacoustics*, Vol. 17, No. 6-8, 2018, pp. 600–623. doi:10.1177/1475472X18789001.

[8] Daroukh, M., Moreau, S., Gourdain, N., Boussuge, J.-F., and Sensiau, C., "Tonal Noise Prediction of a Modern Turbofan Engine With Large Upstream and Downstream Distortion," *Journal of Turbomachinery*, Vol. 141, No. 2, 2019, p. 021010. doi:10.1115/1.4042163.

[9] Morfey, C. L., and Fisher, M. J., "Shock-Wave Radiation from a Supersonic Ducted Rotor," *The Aeronautical Journal of the Royal Aeronautical Society*, Vol. 74, No. 715, 1970, pp. 579–585. doi:10.1017/S0001924000049095.

[10] McAlpine, A., and Fisher, M. J., "On the prediction of "buzz-saw" noise in aero-engine inlet ducts," *Journal of Sound and Vibration*, Vol. 248, No. 1, 2001, pp. 123–149. doi:10.1006/jsvi.2001.3770.

[11] McAlpine, A., and Fisher, M. J., "On the prediction of "buzz-saw" noise in acoustically lined aero-engine inlet ducts," *Journal of Sound and Vibration*, Vol. 265, No. 1, 2003, pp. 175–200. doi:10.1016/S0022-460X(02)01446-3.

[12] McAlpine, A., Fisher, M. J., and Tester, B. J., ""Buzz-saw" noise: A comparison of modal measurements with an improved prediction method," *Journal of Sound and Vibration*, Vol. 306, No. 3-5, 2007, pp. 419–443. doi:10.1016/j.jsv.2007.04.053.

[13] Kassem, M., and Bennani, A., "A three-dimensional cylindrical model for non-linear propagation prediction in lined intake ducts with uniform flow," *20th AIAA/CEAS Aeroacoustics Conference*, 2014. doi:10.2514/6.2014-3114.

[14] Thisse, J., Polacsek, C., Lewy, S., and Lafitte, A., "Generation and Propagation of Multiple Pure Tones Inside Turbofans at Transonic Regime," *AIAA Journal*, Vol. 53, No. 11, 2015, pp. 3466–3478. doi:10.2514/1.J054007.

[15] Moreau, A., Staggat, M., and Gscheidle, C., "A fast prediction method for rotor buzz-saw noise based on an analytical approach," *25th AIAA/CEAS Aeroacoustics Conference*, 2019. doi:10.2514/6.2019-2641.

[16] Thisse, J., Polacsek, C., Mayeur, J., Khelladi, S., Gloerfelt, X., and Lafitte, A., "Numerical Simulations of Shock-Wave Propagation in Turbofan Intakes," *22nd AIAA/CEAS Aeroacoustics Conference*, 2016. doi:10.2514/6.2016-2879.

[17] Lewy, S., Polacsek, C., and Barrier, R., "Analytical and numerical prediction of harmonic sound power in the inlet of aero-engines with emphasis on transonic rotation speeds," *Journal of Sound and Vibration*, Vol. 333, No. 26, 2014, pp. 7165–7182. doi:10.1016/j.jsv.2014.06.013.

[18] Cambier, L., Heib, S., and Plot, S., "The Onera elsA CFD software: input from research and feedback from industry," *Mechanics & Industry*, Vol. 14, No. 3, 2013, pp. 159–174. doi:10.1051/meca/2013056.

[19] Launder, B. E., and Sharma, B. I., "Application of the energy-dissipation model of turbulence to the calculation of flow near a spinning disc," *Letters in Heat and Mass Transfer*, Vol. 1, No. 2, 1974, pp. 131–137. doi:10.1016/0094-4548(74)90150-7.

[20] Thompson, K. W., "Time Dependent Boundary Conditions for Hyperbolic Systems," *Journal of Computational Physics*, Vol. 68, No. 1, 1987, pp. 1–24. doi:10.1016/0021-9991(87)90041-6.

[21] Peters, A., Spakovszky, Z. S., Lord, W. K., and Rose, B., "Ultrashort Nacelles for Low Fan Pressure Ratio Propulsors," *Journal of Turbomachinery*, Vol. 137, No. 2, 2014, p. 021001. doi:10.1115/1.4028235.

[22] Polacsek, C., Chelius, A., Daroukh, M., François, B., and Barrier, R., "Tone noise prediction of a full-scale UHBR engine with short inlet and inflow distortion," *25th International Congress on Sound and Vibration*, 2018.

[23] Cantrell, R. H., and Hart, R. W., "Interaction between Sound and Flow in Acoustic Cavities: Mass, Momentum, and Energy Considerations," *The Journal of the Acoustical Society of America*, Vol. 36, No. 4, 1964, pp. 697–706. doi:10.1121/1.1919047.

[24] Guérin, S., "Farfield Radiation of Induct-Cutoff Pressure Waves," *23rd AIAA/CEAS Aeroacoustics Conference*, 2017. doi:10.2514/6.2017-4037.

[25] Polacsek, C., Burguburu, S., Redonnet, S., and Terracol, M., "Numerical Simulations of Fan Interaction Noise using a Hybrid Approach," *AIAA Journal*, Vol. 44, No. 6, 2006, pp. 1188–1196. doi:10.2514/1.10688.

[26] Reboul, G., Polacsek, C., Billonnet, G., and Roux, J.-M., "Prediction of BPF tones emitted by the inlet of an aero-engine model using in-duct angular mode spectrum measurements," *20th AIAA/CEAS Aeroacoustics Conference*, 2014. doi:10.2514/6.2014-3105.

[27] Ffowcs Williams, J. E., and Hawkings, D. L., "Sound generation by turbulence and surfaces in arbitrary motion," *Philosophical Transactions of the Royal Society of London A*, Vol. 264, No. 1151, 1969, pp. 321–342. doi:10.1098/rsta.1969.0031.

[28] Lewy, S., "Computation of Broadband Noise Radiated by a Ducted Fan in a Uniform Flow," *International Journal of Acoustics and Vibration*, Vol. 8, No. 4, 2003, pp. 211–218.